

ION-BEAM-INDUCED MIXING PROCESSES
AND GAS SPUTTERING

by

RICHARD G. NEWCOMBE, B.Sc. (PHYSICS)

PART B: OFF-CAMPUS PROJECT* (SALFORD UNIVERSITY, U.K.)

A Report

Submitted to the School of Graduate Studies
in Partial Fulfilment of the Requirements
for the degree

Master of Engineering

Department of Engineering Physics
McMaster University
Hamilton, Ontario, Canada

August, 1980

*One of two Project Reports: The other part is designated
PART A: ON-CAMPUS PROJECT

MASTER OF ENGINEERING (1980)
Department of Engineering Physics

MCMASTER UNIVERSITY
Hamilton, Ontario

TITLE: Ion-Beam-Induced Mixing Processes and Gas Sputtering

AUTHOR: Richard G. Newcombe, B. Sc. (McMaster)

SUPERVISOR: Off-Campus: Professor G. Carter, University of Salford
On-Campus: Dr. D. A. Thompson, McMaster

NUMBER OF PAGES: viii, 45

ACKNOWLEDGEMENTS

I wish to thank my off-campus supervisor, Professor G. Carter^(a), for all his direction and guidance while I was at Salford. All the members of his research group^(a) were also of much help, especially Dr. C. Christodoulides, Dr. D. Armour, Dr. D. Ingram, R. Webb and P. Tognetti.

Thanks are also due to Dr. D. A. Thompson^(b), Dr. J. A. Davies^(c) and Dr. G. Fischer^(b) for useful discussions during the writing of this report.

- (a) Department of Electrical Engineering, University of Salford, Salford M5 4WT, Lancashire, U.K.
- (b) Department of Engineering Physics, McMaster University.
- (c) Solid State Branch, Atomic Energy of Canada, Chalk River, Ontario.

ABSTRACT

Section I of this report discusses ion-beam induced mixing processes in solid targets. It is shown theoretically that cascade mixing can be approximated as a diffusion process. Further calculations attempt to show that some of the phenomena of ion-plating can be explained by this mixing process. Experimental data was obtained on the mixing of thin (~200 nm) layers of Ag into a Si substrate by bombardment with 35keV Ar⁺ ions, at fluences up to 6×10^{14} ions/mm². The results were observed by 2.0 MeV He⁺ ion Rutherford back-scattering.

In Section II, the release of trapped Kr from Ni is discussed. Kr, doped with radioactive ⁸⁵Kr*, was implanted as 20keV ions, and subsequently released by post-bombardment with 5keV, 20keV and 80keV Kr⁺ ions. Three sets of Ni samples were Kr implanted to fluences of 5×10^{12} ions/mm², 5×10^{13} ions/mm², or 5×10^{14} ions/mm². The post-bombardment was carried out to fluences ranging from 5×10^{12} ions/mm² to 3.5×10^{14} ions/mm². The relative quantities of trapped Kr* were determined by counting radioactive decay events for a fixed time interval.

The results of this preliminary work show that many more experiments are required before these processes can be well-understood.

TABLE OF CONTENTS

Page No.

Section I: Ion-Beam Induced Mixing Processes

Chapter 1)	<u>Introduction</u>	1
Chapter 2)	<u>Theory</u>	
	§2.1: Radiation Enhanced Diffusion	3
	§2.2: Recoil Implantation	3
	§2.3: Collision-Cascade Mixing	4
	§2.4: Ion-Plating	8
	§2.5: Rutherford Backscattering	10
Chapter 3)	<u>Experimental Technique</u>	
	§3.1: Sample Preparation	13
	§3.2: Ion Implantation Facility	13
	§3.3: Rutherford Backscattering Facility	14
Chapter 4)	<u>Results and Discussion</u>	15
Chapter 5)	<u>Conclusions</u>	19

Section II: Ion-Beam Induced Gas Release Processes

Chapter 1)	<u>Introduction</u>	20
Chapter 2)	<u>Theory</u>	21
Chapter 3)	<u>Experimental Techniques</u>	23
Chapter 4)	<u>Results and Discussion</u>	24
Chapter 5)	<u>Conclusions</u>	30

<u>Tables and Figures</u>	<u>Page No.</u>
Table I: The Sputtering of Ag Films with 35keV Ar ⁺ Ions	31
Table II: Krypton Release Cross-Section and Relative Trapping	32
Table III: Distance and Depth Parameters for Kr ⁺ Ions Incident on Ni	33
Table IV: Dose Effects Upon Rare Gas Implant Distribution	34
Figure 1: Collision Cascade	35
Figure 2: Ion-Plating Profiles	35
Figure 3: RBS Spectra: a) Ag film on Si b) CuAu film on Si	36
Figure 4: Schematic Diagram of Evaporation System	36
Figure 5: Schematic Diagram of Salford Isotope Separator	37
Figure 6: Schematic Diagram of Salford RBS Facility	37
Figure 7: Low Incidence Angle RBS Spectra: a) 10 ^o b) 15 ^o	38
Figure 8: RBS Spectra of Ag Films	38
Figure 9: RBS Spectrum of Ag on Si, after 6x10 ¹⁴ ions/mm ² of 35keV Ar ⁺	39
Figure 10: Estimated Depth Profile of Ag in Si after 6x10 ¹⁴ ions/mm ² of 35keV Ar ⁺	39
Figure 11: Collection Curve of 20keV Kr ⁺ in Ni	40
Figure 12: Desorption Spectrum of 500eV Ar ⁺ Implanted into Ni	40
Figure 13: Sputtering of Ni with 40keV Kr ⁺ , McMaster	40
Figure 14: ⁸⁵ Kr* Release by Kr ⁺ Post-Bombardment	41
Figure 15: 20keV Post-Bombardment of 5x10 ¹³ ions/mm ² Implant, Calculations	41
Figure 16: Sputtering of Ni with 40keV Xe ⁺ , Salford	42

	<u>Page No.</u>
Figure 17: RBS Spectra of 40keV Xe ⁺ in Ni	42
Figure 18: Kr ⁺ Ion Profiles in Ni(Winterbon Calculations)	42
Figure 19: Changes In Trapped Rare Gas Profiles with Implant Fluence	43
Figure 20: Comparison of 80keV Kr ⁺ Energy Deposition Profile with Adjusted 20keV Kr ⁺ Deposition Profile	43
References	44

SECTION I: ION-BEAM INDUCED MIXING PROCESSES

CHAPTER 1

INTRODUCTION

Ion-beam sputtering is often used for cleaning surfaces of contaminants, for sputter-machining, and for sputter-profiling when used in conjunction with surface analysis techniques such as Auger-electron spectroscopy. However, the ion beam does not have the ideal property of removing the surface uniformly, layer by layer.¹ Complicating factors include changes in the surface topography, preferential sputtering, and ion-beam induced mixing. The latter two can alter the composition versus depth profile.

The kinetic energy of the ions is largely deposited in the outermost few tens of nanometers of the target, depending upon the ion energy, and the atomic mass and atomic number of both the ions and the target atoms. The energy (E) is deposited into ionization and electronic excitation through inelastic collisions, and into atomic displacements through elastic collisions. Normally, the energy deposited in the surface 0.5 - 1.0 nm is responsible for sputtering. Energy deposited in elastic collisions is responsible for some mixing of target atoms. This mixing can be the result of direct recoil

mixing² or enhanced diffusion due to increased concentration of defects.³

CHAPTER 2

THEORY

§ 2.1 Radiation Enhanced Diffusion

The main diffusion processes require the presence of defects, such as vacancies and interstitials. Under ion-beam irradiation, large concentrations of defects can develop. Near defect sinks such as grain boundaries and dislocations, large gradients of defects can develop. These factors allow diffusion to occur much faster than it would in relatively defect-free material.

§ 2.2 Recoil Implantation

In the elastic collisions between incident ions and target atoms, kinetic energy is transferred to target atoms. This energy causes some of them to recoil. In the case of very thin films (thinner than about twice the range of the incident ions), recoil implantation will occur if the film atoms tend to recoil deeper into the substrate than substrate atoms recoil. For example, light atoms have a larger range than heavier atoms of the same energy. Therefore a film of light atoms on a heavier

substrate may show recoil implantation. This also depends on the atomic mass of the incident ions and the target atoms, since the energy transferred in a collision depends on the relative masses of the colliding bodies. The target atoms which are closer in mass to the incident ions will receive more energy, and hence have a greater range. However, this latter effect only applies to atoms recoiling from a collision with the incident ion. For 35keV Ar⁺ in Ag, only a small fraction of recoils result from direct collisions with the incident ions; most recoils are from higher order collisions. See references 2,5,6 for greater detail.

§2.3 Collision-Cascade Mixing

Atoms which recoil from collisions with incident ions travel some distance in the solid, creating further displaced atoms, which in turn displace other atoms, etc. Hence, each ion creates a cascade of displaced atoms in the target. As mentioned above, the majority of these displaced atoms are produced by the higher order collisions (secondary, tertiary, etc.). For this reason they have a low energy, and may move only a few atomic spacings. Because of the statistical nature of the collision events, the motion of these low energy atoms is essentially isotropic, except near a surface.

Sigmund⁷ gave the approximate number of displaced atoms per ion as

$$N_d = 0.42\nu(E)/E_d \quad (1)$$

where $\nu(E)$ is the fraction of the incident ion energy deposited

in elastic collisions, and E_d is the average energy needed to displace an atom far enough from its site that it will not immediately be re-trapped by that site. For metals, E_d is approximately 25eV. For example, when a 35keV Ar^+ ion is incident upon Ag, $v(E) \approx 20\text{keV}$, $N_d \approx 21\text{eV}$, and therefore $N_d \approx 400$ displacements/ion. The mean range, or penetration depth, is about 7nm. If the incident ion fluence is 10^{12} ions/ mm^2 , then the number of displacements is of the order $10^{19}/\text{mm}^3$. Since the atomic number density of Ag is $6 \times 10^{19}/\text{mm}^3$, this means that a very large fraction of the atoms in the region of the collision-cascades suffer at least one displacement. If each displacement moves an atom by about one nanometer, this small ion fluence may result in a good deal of mixing.

Haff and Switkowski⁸ attempted to describe this mixing with a diffusion model. The basis of their model is the assumption that displaced atoms in a cascade behave similarly to diffusing gas atoms, for the duration of the cascade. They developed the gas diffusion coefficient:

$$\left. \begin{array}{l} D = \ell^2/3\tau \\ v = \ell/\tau \end{array} \right\} D = \frac{1}{3} v\ell \quad (2)$$

where ℓ is the mean recoil distance, τ is the lifetime of the cascade ($\approx 10^{-13}$ sec), and v is the mean velocity of a recoil in the cascade. They multiplied D by f , the fraction of atoms displaced during the cascade:

$$D_{\text{eff}} = \frac{1}{3} v\ell f. \quad (3)$$

They made the approximation that $v \approx d/\Delta T$ (4)

where d is the cascade diameter (assuming a cylindrical cascade) and ΔT is the time between successive cascades at any one point.

Using $\Delta T = (Jd^2)^{-1}$ (5), where J is the ion flux, then $Jd^3 \approx v$. (6)

They showed that

$$f \approx \left(\frac{dE}{dx} \right)_n / 2E_d d^2 N \quad (7)$$

where $(dE/dx)_n$ is the rate of loss of ion energy through elastic collisions, i.e. the nuclear stopping, and N is the number density of target atoms. Thus,

$$D = \frac{1}{6} \frac{J \ell d}{E_d N} \left(\frac{dE}{dx} \right)_n \quad (8)$$

Andersen⁹ used a slightly different model. He took Einstein relation, $D = \frac{1}{6} v \ell^2$ (9)

where v is the jump (displacement) frequency. At the rate v , in time t , the average atom is displaced η times, where

$$v = \eta/t. \quad (10)$$

Andersen derived η in a similar fashion to Haff and Switkowski's derivation of f .

Carter et al.⁴ took another slightly different approach. They used equation 8, as did Andersen, but calculated that

$$\begin{aligned} v &= \frac{\text{number of displacements/sec}}{(\text{volume of cascade})(N)} \\ &= Jn(E)/NR^3 \end{aligned} \quad (11)$$

where $n(E)$ is the number of displacements per ion, and R is a cascade range parameter, of the order of the projected range of the ion.

Haff and Switkowski⁸, using conservative estimates of d and λ , found that for 500keV Ar^+ ions incident upon Cu, and an ion flux of 6×10^{12} ions/mm²sec ($1\mu\text{A}/\text{mm}^2$), then $D \approx .08 \text{ nm}^2/\text{sec}$.

Andersen⁹, and Carter et al.⁴ calculated the broadening of a delta function impurity distribution into a Gaussian distribution with width

$$\sigma = \sqrt{4Dt} \quad (12)$$

in the time t that it takes to sputter off a layer of thickness R . Andersen found that the full-width at half-maximum was

$$\Delta_{\text{FWHM}} \approx 2\lambda\sqrt{vt} = 2\lambda\sqrt{\frac{n(E)}{Y}} \quad (13)$$

where Y is the sputtering yield, atoms/ion. Carter et al.⁴ got the equivalent,

$$\sigma = \sqrt{\frac{4n(E)}{6Y}} \lambda \quad (14)$$

However, Carter et al.⁴ showed that this equation is not always valid. It implicitly assumes that σ , the broadening, is much less than the sputtered depth, R . For 500keV Ar^+ incident on Cu, R will be of order 50nm, $n(E)$ will be of order 10,000, and Y will be of order 5. Taking λ to be about 1nm, as Andersen⁹ did, gives $\sigma \approx 35\text{nm}$, which is 70% of R . Therefore, the broadening would occur so rapidly that the approximation for σ would be only marginally valid.

Tsaur et al.¹⁰ have recently performed experiments to find ion-beam induced broadening in Pt layers in Si, and in Si layers in Pt. They fitted their results to their own version of the above diffusion models, concluding that λ should be $\approx 3\text{nm}$ for Pt in Si, and $\approx 8.5\text{nm}$ for Si in Pt. They linked these to the host lattice displacement energy,

$$\frac{E_d(\text{Si})}{E_d(\text{Pt})} \approx \frac{13\text{eV}}{36\text{eV}} \approx .36 \approx \frac{3\text{nm}}{8.5\text{nm}} \quad (15)$$

It should be noted that the low energy recoils would not be expected to have a range as large as 3nm, unless they travel diffusively, perhaps along dislocations or grain boundaries.

§2.4 Ion-Plating

In ion-plating, films are deposited in a relatively high-pressure glow-discharge environment. For example, the substrate may form the cathode of a 2kV discharge, in 1 Pa of rare gas (e.g. Ar), into which the film material is either evaporated or sputtered. As a result of this, the substrate is bombarded with a very high flux of ions and atoms with a range of energies. For a 2kV discharge, the peak energy of the distribution is about 500eV. In many cases, the interface region between the pure substrate and pure deposited material is broadened considerably; more than can be accounted for by either direct ion implantation¹¹, or recoil implantation¹². This can be a very desirable effect, since the film adhesion is improved if the interface region is wide.

Armour et al.¹³ suggested that the interface broadening may be largely due to enhanced (effective) diffusion in the region affected by the energetic ion and atom bombardment. Atoms which may be normally insoluble in the substrate can be forced into it by ion bombardment. Their deposited energy creates cascade mixing of the film and substrate atoms, as discussed in §2.3.

$$\text{Armour et al.}^{13} \text{ used } v = \frac{J\bar{\theta}(E,x)}{N} \frac{0.42}{E_d} \quad (16)$$

where $\bar{\theta}(E,x)$ is a depth distribution of the energy deposited in elastic collisions, approximate because E is really a spectrum of energies, not a unique energy. Then, following equation 9,

$$D(x) = \frac{1}{6} v \ell^2 = \frac{(.42) J \bar{\theta}(E,x) \ell^2}{6 N E_d} \quad (17)$$

When the film becomes much thicker than the maximum range of the energetic ions and atoms, the value of D will drop off. Assuming that the film grows at a constant rate:

$$\rho = dx/dt, \quad (18)$$

the inward diffusion of the film may be calculated by treating it as the broadening of a delta function, with a decaying diffusion coefficient. This results in an inward broadening width of

$$\Delta x \approx \frac{1}{2} \left(\frac{J}{J_\tau} \frac{\ell^2 \lambda \bar{\theta}(E,0)}{E_d C} \right)^{1/2} \quad (19)$$

where Δx is like the σ of a Gaussian, J/J_τ is the ratio of

energetic ions and atoms to thermal atoms, incident upon the substrate, C is the sticking coefficient for the thermal atoms, λ is a decay distance for the deposited energy distribution, and $\bar{\theta}(E,0)$ is the energy deposited at the surface through elastic collisions. For a typical Ar discharge at 2kV, with a current density of $10\mu\text{A}/\text{mm}^2$, $\rho \approx 1\text{nm}/\text{sec}$, and $J/J_\tau \approx .5$, the average energetic particle would have about 500eV. Taking $\ell \approx 2-3a_0$, $\lambda \approx 2-3a_0$, $\bar{\theta}(E,0) \approx 100\text{eV}/\text{atom layer}$, and $E_d \approx 25\text{eV}$, they found $\Delta x \approx 3a_0$, where a_0 is one atomic spacing.

Assuming that the outward broadening is approximately equal to the inward broadening, $\Delta x \approx 6a_0$, or about 2nm. This kind of broadening has been observed experimentally.¹⁴

Under conditions of higher discharge potentials, larger J/J_τ ratios, and initially low deposition rates, it is conceivable that the outward broadening could be considerably larger than the inward broadening, resulting in a sequence of profiles like figure 2.

§2.5 Rutherford Backscattering

The main tool for analysis of surfaces used for this report is Rutherford backscattering. MeV He^+ ions collide with atoms in a way which is described extremely well by the Rutherford model. The collisions are elastic, Coulombic collisions between the He nuclei and the target nuclei. Without

the small correction for electronic screening of the nuclear charge in the case of high atomic number target atoms³⁰, the Rutherford differential scattering cross-section is given by

$$\frac{d\sigma}{d\omega} = 1.296 \times 10^{-25} \left(\frac{Z_1 Z_2}{E_0} \right)^2 \left(\frac{M_1 + M_2}{M_2} \right)^2 \sin^{-4} (\theta_s/2) \quad (20)$$

where $d\sigma/d\omega$ is the scattering cross-section of incident ions of atomic mass M_1 , atomic number Z_1 , and initial energy E_0 , scattered by a target atom of atomic mass M_2 , atomic number Z_2 , into a unit solid angle at center-of-mass scattering angle θ_s . E_0 is in MeV, in order to give $d\sigma/d\omega$ in $\text{mm}^2/\text{steradian}$.

The total number of scattered ions detected is

$$S = (N\Delta x)n\left(\frac{d\sigma}{d\omega}\right)\Delta\omega \quad (21)$$

where $N\Delta x$ is the areal density of target atoms (atoms/mm^2), n is the fluence of incident ions (ions/mm^2) and $\Delta\omega$ is the solid angle subtended by the detector (steradians).

He^+ ions which are backscattered by the surface monolayer will have an energy dependent on the mass of the He^+ ion and that of the target atom, according to

$$E_1 = k^2 E_0 = \left(\frac{M_1 \cos \theta_L + M_2}{M_1 + M_2} \right)^2 E_0 \quad (22)$$

where, now, θ_L is the scattering angle in laboratory coordinates. Therefore one can identify a target atom by the energy of He^+ ions which scatter from it through a well-defined, known angle.

Ions which penetrate beneath the surface will steadily lose energy through electronic excitation and ionization, before and after being backscattered. If the rate of

energy loss as a function of energy is known, the energy spectrum of the backscattered ions can be converted to a depth profile of the target atoms. For two examples, see Figures 3a, 3b. For more detail, see reference 16.

CHAPTER 3

EXPERIMENTAL TECHNIQUE

The experimental part of this project was performed at Salford University, Salford, U.K.

§3.1 Sample Preparation

The samples consisted of thin (~200nm) films of Ag evaporated onto polished, cleaned, single crystal Si wafers. The base pressure of the evaporator was about 3×10^{-4} Pa. The Ag was evaporated from a tungsten filament. See figure 4.

§3.2 Ion Implantation Facility

The samples were bombarded with 35keV Ar^+ ions in the Salford isotope separator, to fluences from 10^{14} ions/mm² to 6×10^{14} ions/mm², at a flux of about $.1\mu\text{A}/\text{mm}^2$. The pressure of the target chamber during the ion bombardment was about 10^{-4} Pa.

The ions were mass-energy analyzed by passing through a 60° magnet and several defining apertures. Ions with the wrong charge-to-mass ratio, or energy, hit the beam-line walls or the apertures. See Figure 5.

§3.3 The Rutherford Backscattering Facility

The samples were analyzed before and after the implantations by Rutherford backscattering of 2.0MeV He⁺ ions from the Salford Van de Graaf accelerator. The ion beam was highly collimated by passing it through three successive small apertures. The ions were backscattered through 168° into a surface barrier detector, the output of which was pulse-height analyzed, giving an energy spectrum of backscattered particles. The incidence angle of the ion beam to the target surface was carefully set by means of a fixed laser beam and a high-precision goniometer.

The scattering geometry is shown in Figures 6 and 7: in all cases, $\theta_L = 168^\circ$. The 90° incidence analysis gave a depth equivalent per channel of 4.7nm, in the Ag peak. The low angle incidence analysis provided greater depth resolution: 1.2nm/channel at 10°, and 1.7nm/channel at 15°. This is because the He⁺ ion must travel through more target material in going to and from the same scattering depths: at 90° incidence, it travels through $\Delta x + \Delta x / \cos 12^\circ$; at 10° incidence, it travels through $\Delta x / \cos 80^\circ + \Delta x / \cos 68^\circ$, which is four times as far as the 90° incidence case. Therefore the ion loses more energy in going to the same depth. At a constant energy per channel, (5keV), this results in a greater depth resolution.

CHAPTER 4
RESULTS AND DISCUSSION¹⁶

The depth scales of the Rutherford backscattering spectra (RBS spectra) were calculated from the equation:

$$\Delta z = \Delta E \left[\frac{k^2 S(E_0)}{\cos \theta_1} + \frac{S(k^2 E_0)}{\cos \theta_2} \right]^{-1} \quad (23)$$

where $\Delta E = 5\text{keV}$ per channel, Δz is the depth equivalent per channel, $S(E)$ is the stopping power (electronic slowing) of the target material, and θ_1 and θ_2 are the angles given in figure 7. $k_{\text{Ag}}^2 = .8635$, so $k_{\text{Ag}}^2 E_0 = 1.727\text{ MeV} =$ the energy of a He^+ ion which is backscattered from a Ag atom on the surface. In a Ag film, $S(E_0) \approx .53\text{ keV/nm}$, and $S(k^2 E_0) \approx .58\text{keV/nm}$. This gives the above mentioned depth scale at 10° incidence of $\Delta z = 1.2\text{nm/channel}$. This constant value of Δz applies for about the outermost 100nm of the Ag film. As the beam reaches greater depths, the scattering cross-section increases, because it varies inversely with the particle energy, as shown in equation 20. This can be seen in Figure 8, in the RBS spectra of Ag: the peak height increases with decreasing energy.

Using Δz , one can approximate the thickness of the films from the number of channels corresponding to the peak width, as given in Table I. From the change in thickness of the

film as a function of ion fluence, the sputtering yield can be determined. As Table I shows, the sputtering yield varied somewhat. Its average value was about 12 atoms/ion, slightly less than a value of 14 interpolated from Andersen and Bay's¹⁷ work. The reason for these variations might be found in the fact that the samples were not analyzed in situ. Between each Ar⁺ implantation, the samples were exposed to atmosphere for periods of days, during which time the surface would have been contaminated.

After a fluence of 6×10^{14} ions/mm², the surface film of Ag was essentially sputtered away. It was observed that the Ag peak was about 35% of the height of the unsputtered (virgin) peak (see Figure 8), and that the Si peak had a reduced height in the region corresponding to the surface (see Figure 9). The Si peak was no longer shifted to lower energy, as it had been when there were Ag films of various thickness covering the Si. The energy of the Ag peak showed that it was at or near the surface. Therefore it was concluded that the surface region of the Si substrate contained large amounts of Ag. The surface concentration of Ag was confirmed to be in the range of 20% - 35% by a subsequent Auger analysis at McMaster University.

The depth profile of Ag in Si (see figure 10) was estimated using the technique developed by Christodoulides et al.¹⁸, in which the height of the Si peak relative to the height of a virgin Si peak gives an indication of the relative

stopping powers, from which one can determine the altered depth per channel for the Ag peak. This assumes a flat, uniform surface. However, the surface of the sample bombarded to 6×10^{14} ions/mm², as seen in the scanning electron microscope, showed "pebbling", i.e. bumps of 100nm - 200nm diameter. For this reason the depth-profile must be considered as semi-quantitative. However, the extracted profile shows that considerable Ag penetrated to a depth of 24nm, i.e. the range of 35keV Ar⁺ ions in 25% Ag, 75% Si.

In similar work on the ion bombardment of Au films on Si, Blank and Wittmaack¹ decided that radiation enhanced diffusion explained the mixing. There is good reason for this, as the defect concentrations at such large ion fluences would be essentially saturated. Furthermore, Si has been observed¹⁹ to migrate through Au at quite low temperatures (200°C). Si has also been seen to migrate through Ag³⁰, although at higher temperatures (400°C). Therefore radiation enhanced diffusion could well be very important in the experiment.

On the other hand, cascade mixing could also be important. Using equation 13:

$$\sigma = \sqrt{\frac{4n(E)}{6Y}} \ell \quad (13)$$

$n(E) \approx \frac{0.42 (E)}{E_d} \approx \frac{(0.42)(20\text{keV})}{E_d} = 400$ displacements per ion,
 $Y = 12$ and $\ell \approx 3\text{nm}$ from Tsauro et al.¹¹, then $\sigma \approx 14\text{nm}$. This

agrees well with the estimated depth profile in Figure 10.

On the basis of present data it is difficult to decide whether diffusion or cascade mixing dominates. On the atomic level, it is difficult to distinguish these processes: a displaced atom may travel several atomic distances violently, because of its collisionally imparted kinetic energy, after which it may diffuse thermally. Since, as Marwick and Piller³ showed, it is very difficult to determine enhanced diffusion coefficients, it is difficult to draw the line between cascade mixing and radiation enhanced diffusion.

CHAPTER 5

CONCLUSIONS

A theoretical model for a diffusion approximation to collision - cascade mixing (§ 2.3) was found to apply to some situations in ion-plating (§ 2.4) and to an experiment in which a 200nm thick film of Ag on a Si substrate was bombarded with a high (6×10^{14} ions/mm²) fluence of 35keV Ar⁺ ions (§ 3.4). However, this model is very approximate, and there is a great scarcity of experimental data for its improvement.

SECTION II: ION BOMBARDMENT INDUCED RELEASE OF KRYPTON IMPLANTED INTO NICKEL

CHAPTER 1

INTRODUCTION

There is a strong interest in the behaviour of rare gases in solids, as evidenced by the numbers of papers on the subject, e.g. the review article by Carter et al.²⁰ It is particularly of interest in fission reactor technology, because large quantities of Kr and Xe are produced in the fission product decay process. Since these atoms are generated with kinetic energy, their behaviour in solids may be simulated by ion-bombardment. As well, ion implantation is being considered as a means of storing the radio-krypton produced as a by-product of fission. This report discusses an experiment in which various fluences of Kr^+ ions, doped with radioactive $^{85}\text{Kr}^*$, were implanted into a simple metal, Ni, then post-bombarded with undoped Kr^+ over a range of energies and fluences. The fraction of the original $^{85}\text{Kr}^*$ remaining was determined by measuring the activity of the sample.

CHAPTER 2

THEORY

Once an ion has entered a solid, there are two major factors which determine η the probability that it will be captured and remain in the solid. One is the trapping probability, which may be expressed as a cross-section, σ_{tr} - it is the probability that the ion will fall into a potential well which can hold it, after it has been slowed to thermal velocities. The other is the release probability, which may also be expressed as a cross-section, σ_r - it is the probability that the trapped atom will be released from the solid by the subsequent impacts resulting from the ion beam. Of course, there is no reason that there cannot be several trapping and release mechanisms, and hence cross-sections. In fact, in most cases, theory and experiment agree that there are many mechanisms, although one or two may dominate. For more detail, see the review article by Carter et al.²⁰

This is a difficult subject to study, theoretically and experimentally. The theory is difficult because it must deal with trapping and release at the atomic level. A great deal of work has been done on building models of metals, and on the trapping of rare gases in metals, but they have had

limited success because of the number of approximations which must be made, in order for a computer to be able to perform the necessary calculations in a realistic time. For examples, see references 20-23.

The experiments are difficult because when, as is usually the case, there are several cross-sections, it is often difficult to distinguish and interpret them. In measuring a saturation (collection) curve, such as figure 11²⁴, the release cross-section(s) must be known before the trapping cross-section(s) can be calculated. In measuring desorption spectra, such as figure 12²⁵, the peak structure is often difficult to interpret.²⁶

Trapping and release will depend upon quantity of Kr which has already been trapped, and its depth distribution. Kr trapped very near the surface may have a greater probability of escaping from the target, because of the shorter distance it has to travel, and the often sharp concentration gradient near the surface. Implanting large quantities of Kr may force some of it into less accessible sites, as the other sites begin to saturate.

CHAPTER 3

EXPERIMENTAL TECHNIQUE

Solid samples of 99.95% pure, polycrystalline bulk Ni were implanted with 20keV Kr^+ ions, doped with .1% $^{85}\text{Kr}^*$, to fluences of 5×10^{12} , 5×10^{13} , and 5×10^{14} ions/ mm^2 in the Salford isotope separator. Their background β -activity had been previously measured. The β -activity of the samples was measured after the radioactive implant, and after each post-bombardment fluence of non-radioactive $^{84}\text{Kr}^+$ ions. The post-bombardment was done at 5keV, 20keV and 80keV, up to fluences of 3.5×10^{14} ions/ mm^2 , in steps of 5×10^{13} ions/ mm^2 or less. The target chamber pressure was about 3×10^{-4} Pa.

CHAPTER 4

RESULTS AND DISCUSSION

Figure 13 shows a plot of $^{85}\text{Kr}^*$ retention versus post-bombardment fluence. The retention scale is in units of $\ln N$, where N is the number of radioactive events counted in a fixed time, minus the background. It is equivalent to a scale of $\ln N_T$, where N_T is the number of $^{85}\text{Kr}^*$ atoms retained. By comparing figure 13 to figure 11 it can be shown that 100 counts correspond to about 4.5×10^{13} atoms/mm² of retained Kr, of which .1% is $^{85}\text{Kr}^*$.

Figure 13 suggests that the release of Kr from Ni is not from one type of site, by a single mechanism; this would be expected to lead to a simple exponential decay law.

It was found, however, that the data could be fitted to a model with two release cross-sections, σ_1 and σ_2 , with no retrapping term, i.e. no term to account for released Kr being trapped again before it escaped the nickel. Taking the two cross-sections as referring to two sites of trapping, the total number of Kr atoms from the initial implant was designated $N_T(t) = N_{1t} + N_{2t}$ (23), or $N_T(\phi) = N_1(\phi) + N_2(\phi)$ (24), where t is time of post-bombardment, and ϕ is the post-bombardment fluence. The release was then described by two simultaneous equations:

$$\frac{dN_1(\Phi)}{d\Phi} = -\sigma_1 N_1(\Phi) \quad (25)$$

and

$$\frac{dN_2(\Phi)}{d\Phi} = -\sigma_2 N_2(\Phi) . \quad (26)$$

For any one implant fluence of $^{85}\text{Kr}^*$, $\frac{N_1(\Phi=0)}{N_2(\Phi=0)} = \alpha$. (27)

Solving (25) and (26) with the boundary conditions (24) and (27) gives:

$$N_T(\Phi) = \frac{N_T(0)}{1 + \alpha} \left(\alpha \exp(-\sigma_1 \Phi) + \exp(-\sigma_2 \Phi) \right). \quad (28)$$

The values of $N_T(\Phi)$ are just the data points in figure 13. The value of σ_2 is approximately the slope of the shallower portions of the $\ln N_T$ vs Φ curves. By extrapolating backwards, one obtains $N_2(0)$, hence $N_1(0) = N_T(0) - N_2(0)$, and hence α . Then, by using these values in equation 28, and by doing some iteration, one can determine values of σ_1 , σ_2 and α which fit the curves (see figure 14). These are given in Table II.

There are, however, several problems with this model. The first is that α would be expected to be independent of the post-bombardment energy. It should be a function only of the implant fluence (of $^{85}\text{Kr}^*$). Table II shows that this is not the case.

The second problem is that the physical sputtering of the nickel has been ignored. As nickel is sputtered from the surface, any Kr trapped at the surface should be released simultaneously. Also, the energy deposition from the post-bombarding ions will be deeper, relative to the original surface, as more of the surface is removed.

The problem of the nickel sputtering turned out to be complicated by the vacuum conditions. At 3×10^{-4} Pa, a layer of oxide will grow on Ni in seconds. As Kelly and Lam²⁷ showed, the sputtering of a metal is almost always slowed when the surface is oxidized. Unless the ion flux is very high, then, the oxide and other contaminants will reduce the sputtering effect upon gas release. In a recent experiment at McMaster University (see Figure 15) it was shown that, in ultra-high vacuum conditions, the initial sputtering rate is slow, but that after several times 10^{13} ions/mm², the sputtering rate of 40keV Kr on Ni is about 6.2 atoms/ions. This is in contrast to a previous experiment at Salford University, by Ingram²⁴, in which he sputtered Ni with 40 keV Xe. He found very little sputtering at fluences of less than 10^{14} ion /mm², rising to a sputtering yield of $Y \sim .4$ atoms/ion at 2×10^{14} ions/mm², and $Y \sim 1.5$ atoms/ion at 5×10^{14} ions/mm². See figure 19. This work was done under similar conditions to the Kr sputtering: the sample was exposed to atmosphere between ion fluences. From this, it seems reasonable to assume that the ⁸⁵Kr* implanted Ni samples were

physically sputtered during post-bombardment, but at a slow, and possibly changing, rate.

If one assumes a sputtering yield of the order of $Y = 1$ atom/ion, and only one trapping site, the data can be explained by accounting for the distribution of deposited energy from the incident ions, relative to the distribution of trapped $^{85}\text{Kr}^*$, in a model similar to that proposed for the release of Kr from Si, Ge and GaAs by Carter et al.²⁹. Table III and figure 17 give the distribution of Kr ions and deposited energy in Ni. However, these values are calculated from Winterbon's²⁸ tables, and do not account for any redistribution of trapped Kr by various processes during the implantation. Ingram's²⁴ results with Xe implanted into Ni show that much redistribution does occur (see Figure 18). The broadening of the rare gas distribution, combined with the release of gas from the surface, may account for the apparent doubling of the mean depth of trapped gas. The distribution of trapped Xe is broadened isotropically in a process which is probably enhanced by the ion bombardment. Any Xe atoms displaced from their traps nearer to the surface than the maximum of the distribution will tend to effectively diffuse down the concentration gradient, and escape from the Ni. Any Xe atoms displaced from their traps deeper in the Ni than the distribution maximum will tend to effectively diffuse down the concentration gradient, deeper into the solid. This is shown pictorially in figure 19.

Assuming that Kr in Ni behaves like Xe in Ni, the change in the Kr distribution as a function of implant dose can be

$$\text{approximated as } \langle x \rangle_{\text{Kr}(\Phi)} \approx \langle x \rangle_{\text{Kr}(0)} \cdot \langle x \rangle_{\text{Xe}(\Phi)} / \langle x \rangle_{\text{Xe}(0)} \quad (29)$$

Table IV gives the results of these calculations.

The revised model holds that the larger rate of release, indicated by the steeper portions of the curves in Figure 13, is due to gas-sputtering, as discussed earlier: Kr which is displaced from its trapping site nearer to the surface than the Kr concentration maximum, immediately diffuses out to the surface, escaping the Ni. The change in release rate at about 5×10^{13} ions/mm² is due to the depletion of Kr from the zone in which energy is being deposited. Thereafter, gas is only released by the deeper portion of the ions' deposited energy distribution, as it moves into the Ni. This motion is due to the slow removal of the surface by physical sputtering.

Since the 5keV energy deposition profile is shallower than the 20keV profile, one would expect that the turnover point would be reached at a lower fluence for 5keV post-bombardment than for 20keV post-bombardment. This is evident in figure 13. The 80keV curves show what could be the beginning of turnover, as expected, at even higher post-bombardment fluences.

The sputtering yield of 20keV Kr should be higher than that of 5keV Kr, since the energy deposited at the surface is larger (see figure 17). Hence, the slower release rate (corresponding to σ_2 in the two-trap model) would be larger for 20keV post-bombardment than for 5keV post-bombardment. This is also seen in Figure 13.

For the low fluence implant (5×10^{12} ions/mm²) the $^{85}\text{Kr}^*$ profile would match the Winterbon ion deposition profile closely, because the implant was small enough to avoid large redistribution effects. Then, as shown by Figure 17, the 20keV energy deposition profile height would be larger in the region of trapped $^{85}\text{Kr}^*$ than the 80keV energy distribution. Therefore one would expect that the gas-sputtering with 20keV ions would be faster than with either the 80keV ions, or the 5keV ions, the latter having a smaller energy deposition than the 20keV ions, everywhere in the solid. This is indicated by the curves in figure 13.

For the higher fluence implants (5×10^{13} ions/mm², 5×10^{14} ions/mm²), the adjusted $^{85}\text{Kr}^*$ profiles would have been deeper by as much as a factor of two, than the 20keV energy deposition profile. Figure 20 shows that the 80keV Kr post-bombardment could be expected to release $^{85}\text{Kr}^*$ faster than either the 5keV or 20keV Kr post-bombardment, because its deposited energy is greater in the region of trapped $^{85}\text{Kr}^*$. Again, this is seen in figure 13.

CHAPTER 5
CONCLUSIONS

The ion-bombardment induced release of Kr from bulk Ni was observed. It was seen to depend upon the energy of the ions and the initial implantation fluence. Two preliminary models were developed in an attempt to describe the release process. Further work is required for a more complete understanding of the process.

TABLE I

The Sputtering of Ag Films with 35 keV Ar⁺ Ions

Ar fluence (ions/mm ²)	Ag peak width (channels)	Ag film thickness (nm)	NΔx of Ag (atoms/mm ²)	S (atoms/ion)
VIRGIN	104	124	7.4x10 ¹⁵	—
1.0x10 ¹⁴	89	106	6.4x10 ¹⁵	10
3.0x10 ¹⁴	69	82	4.9x10 ¹⁵	7.5
6.0x10 ¹⁴	26*	12*	~ 2x10 ¹⁴	16

* At this point the Ag is no longer a separate film, but is mixed into the Si surface

TABLE II

Krypton Release Cross-Sections and Relative Trapping

$^{85}\text{Kr}^*$ doped implant fluence	Post-Bombardment Energy (keV)	σ_1 (\AA^2)	σ_2 (\AA^2)	α
5×10^{14} ions/ mm^2	5	3.0	.154	.174
	20	3.0	.229	.683
	80	—	—	—
5×10^{13} ions/ mm^2	5	3.0	.21	.037
	20	3.0	.28	.524
	80	—	—	—
5×10^{12} ions/ mm^2	5, 20, 80	—	—	—

TABLE III

Distance and Depth Parameters for Kr Ions Incident on Nickel

Energy (keV)	$\langle x \rangle$ (Å)	$\langle x^2 \rangle^{1/2}$ (Å)	$\langle y^2 \rangle^{1/2}$ (Å)	$\langle x_0 \rangle$ (Å)	$\langle x_0^2 \rangle^{1/2}$ (Å)	$\langle y_0^2 \rangle^{1/2}$ (Å)
5	20	10	16	16	10	11
20	53	26	42	42	26	29
80	155	71	122	120	72	79

$\langle x \rangle$ is the mean range of ion penetration

$\langle x^2 \rangle^{1/2}$ is the straggling about that mean range

$\langle y^2 \rangle^{1/2}$ is the transverse straggling about the mean range

$\langle x_0 \rangle$ is the mean damage depth, ie. mean range of energy deposition

$\langle x_0^2 \rangle^{1/2}$ is the damage straggling

$\langle y_0^2 \rangle^{1/2}$ is the transverse damage straggling

TABLE IV

Dose Effects Upon Rare Gas Implant Distributions

Φ (ions/mm ²)	20keV Kr				
	$\langle x \rangle_{Xe}$ (Å) (observed)	$\langle x \rangle$ (Å) (Winterbon)	$\langle x \rangle$ (Å) (adjusted)	$\langle x^2 \rangle^{1/2}$ (Å) (Winterbon)	$\langle x^2 \rangle^{1/2}$ (Å) adjusted
5×10^{12}	~ 70	53	53	26	26
5×10^{13}	~ 100	53	76	26	37
5×10^{14}	~ 150	53	114	26	56

Adjusted values are derived from equation 28.

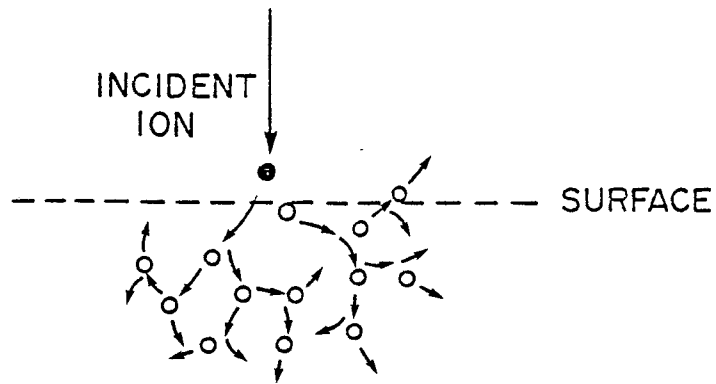


FIGURE 1: Collision Cascade

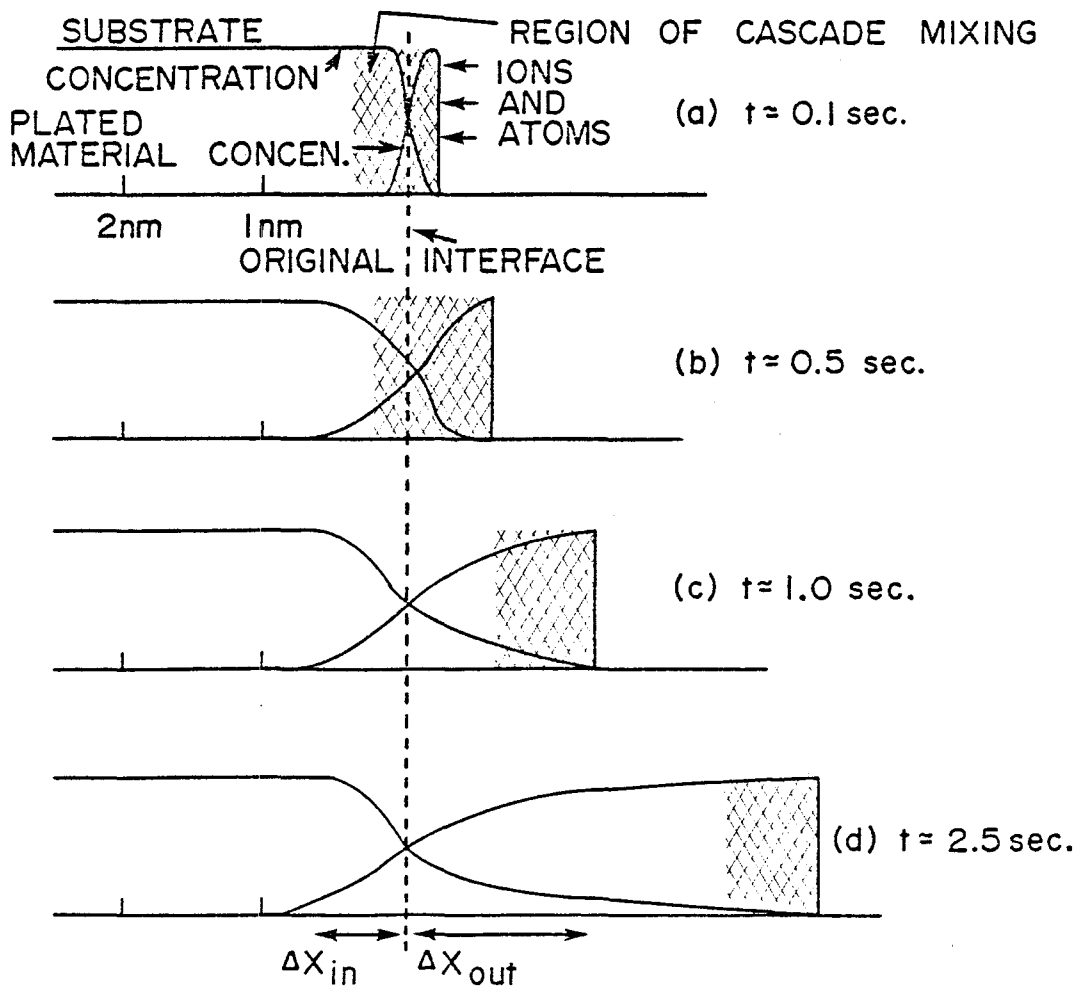


FIGURE 2: Ion Plating Profiles

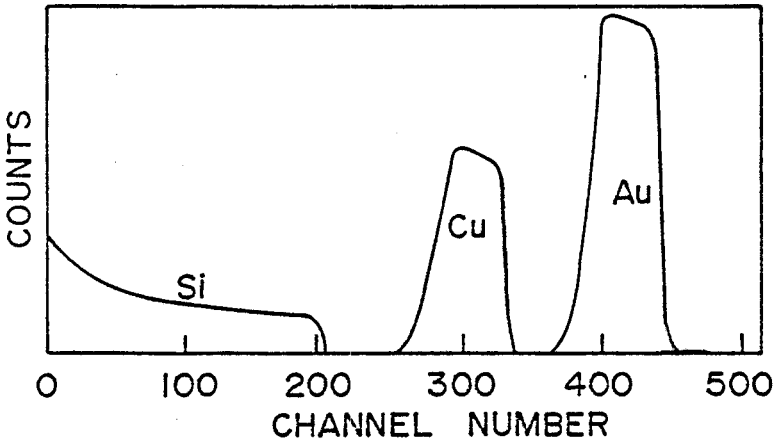
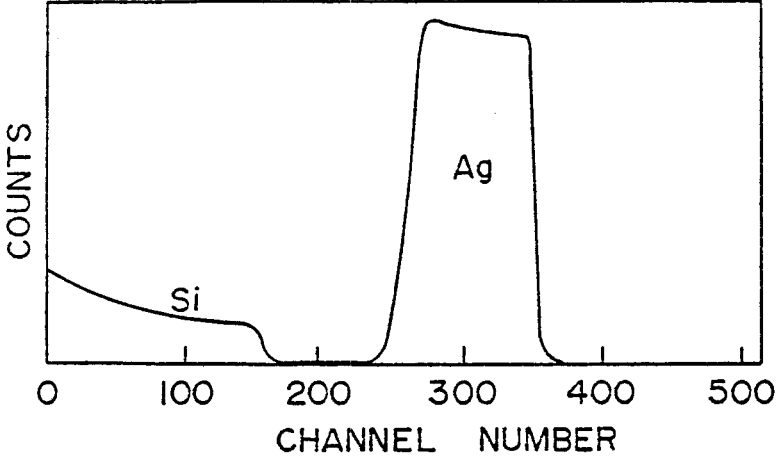


FIGURE 3: RBS Spectra, 2.0MeV He⁺

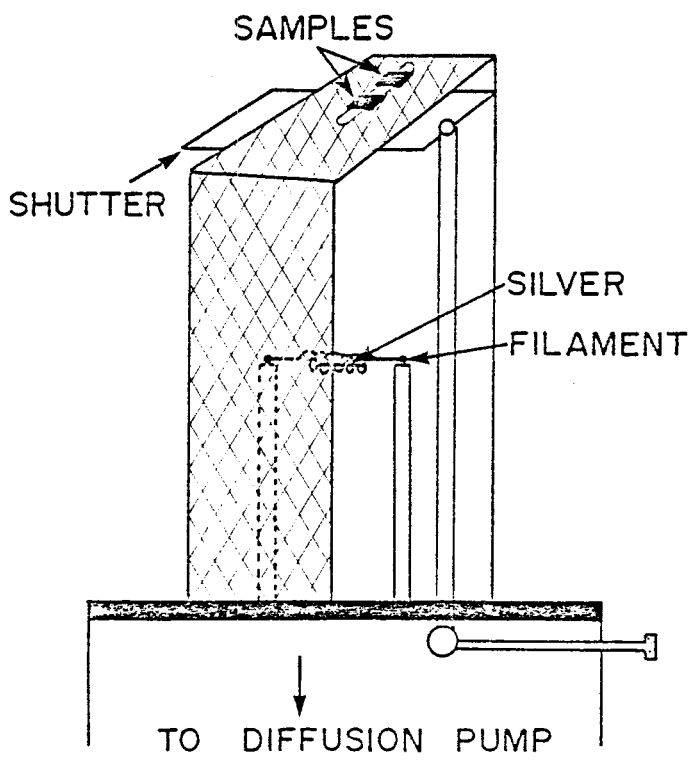


FIGURE 4: Schematic Diagram of Evaporation System

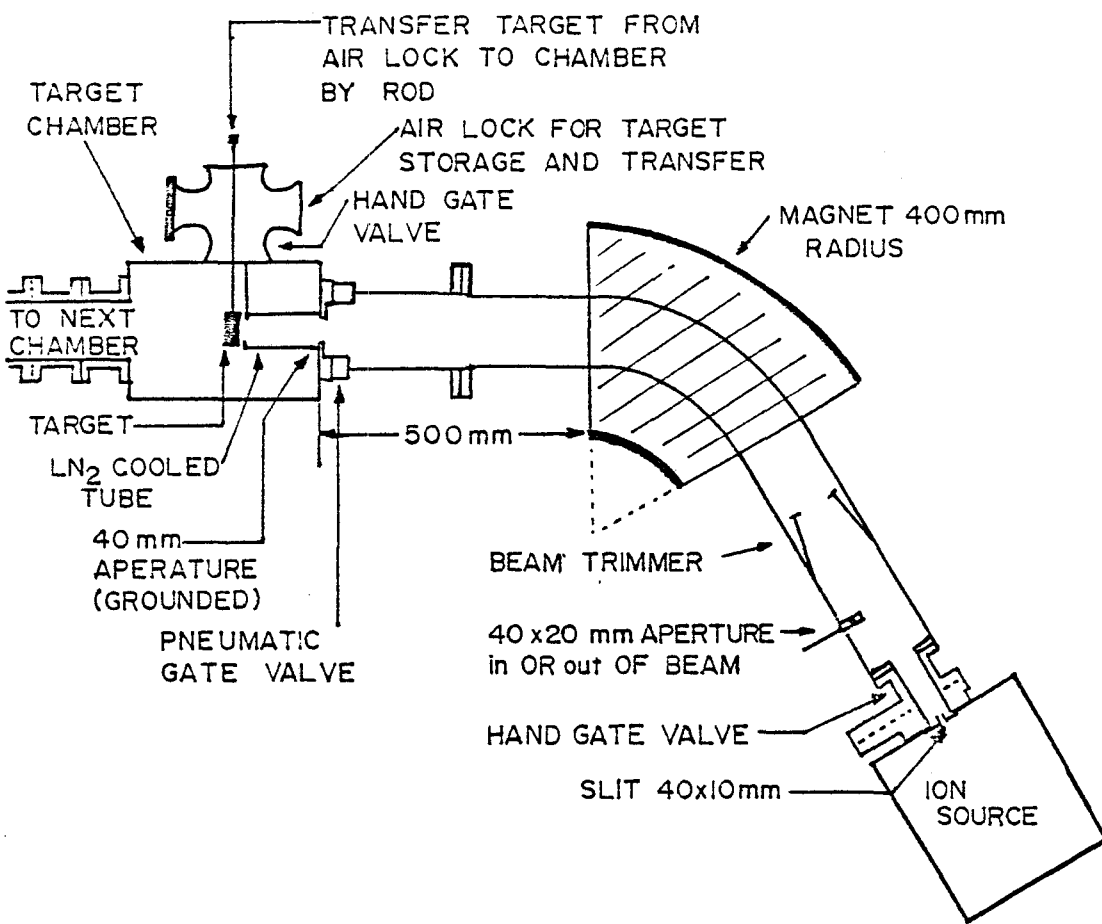


FIGURE 5: Schematic Diagram of Salford Isotope Separator

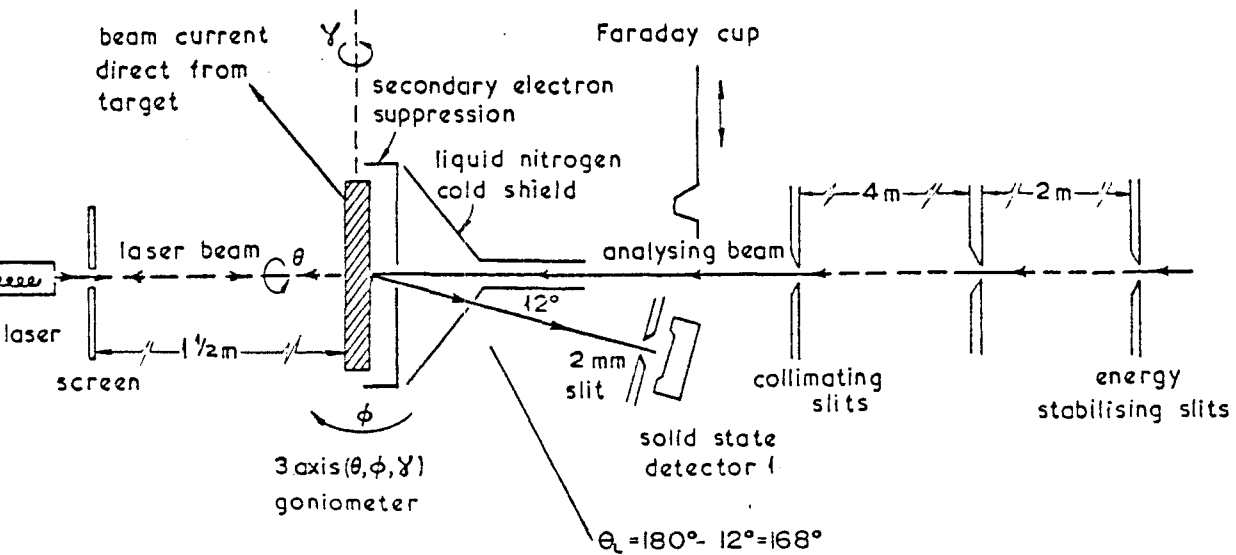
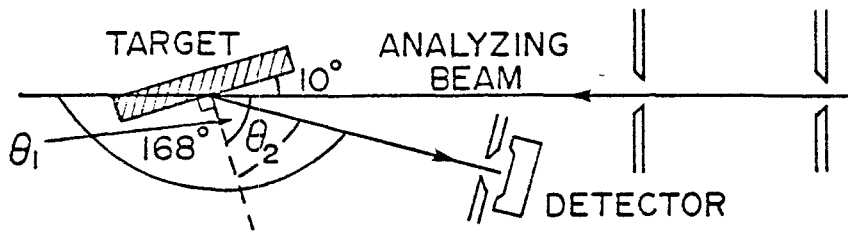
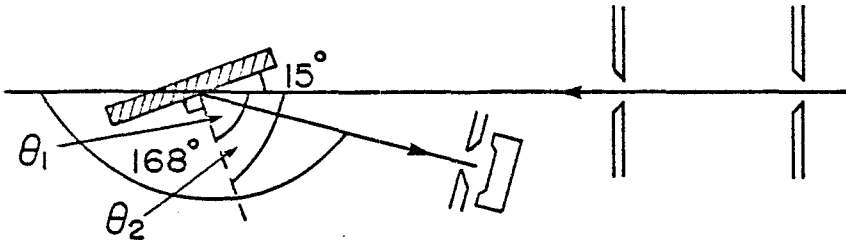


FIGURE 6: Schematic Diagram of Salford RBS Facility



(a) 10° INCIDENT ANGLE RBS ANALYSIS



(b) 15° INCIDENT ANGLE RBS ANALYSIS

FIGURE 7: Low Incidence Angle RBS Spectra

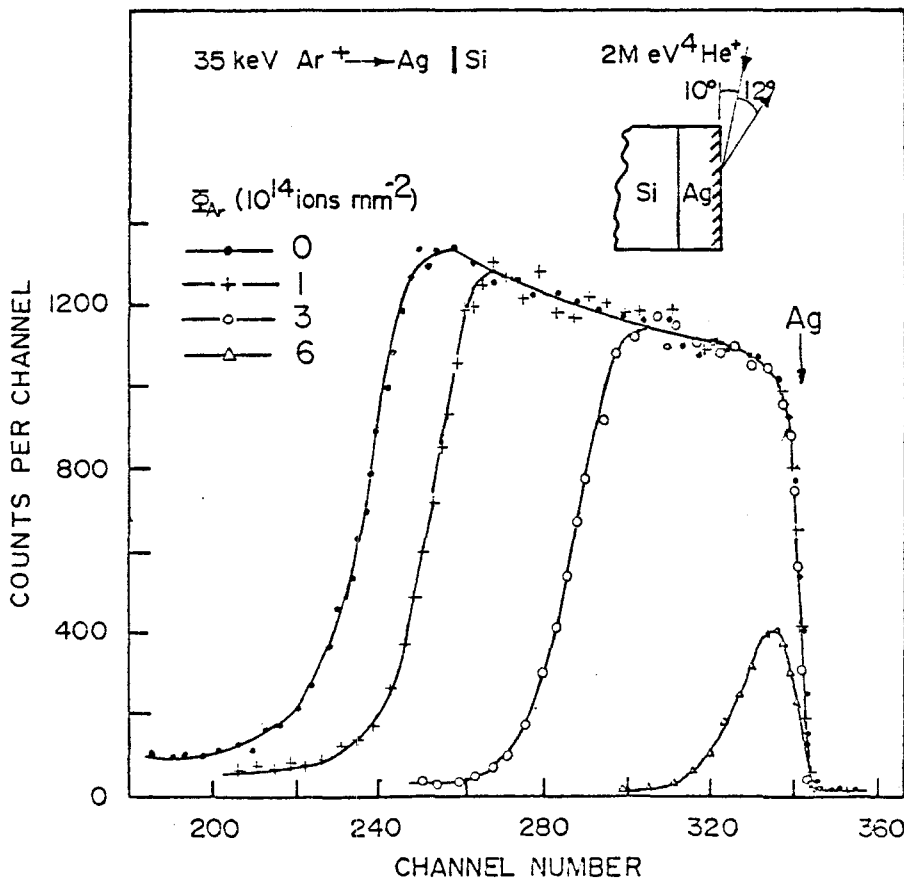


FIGURE 8: RBS Spectra of AG Films

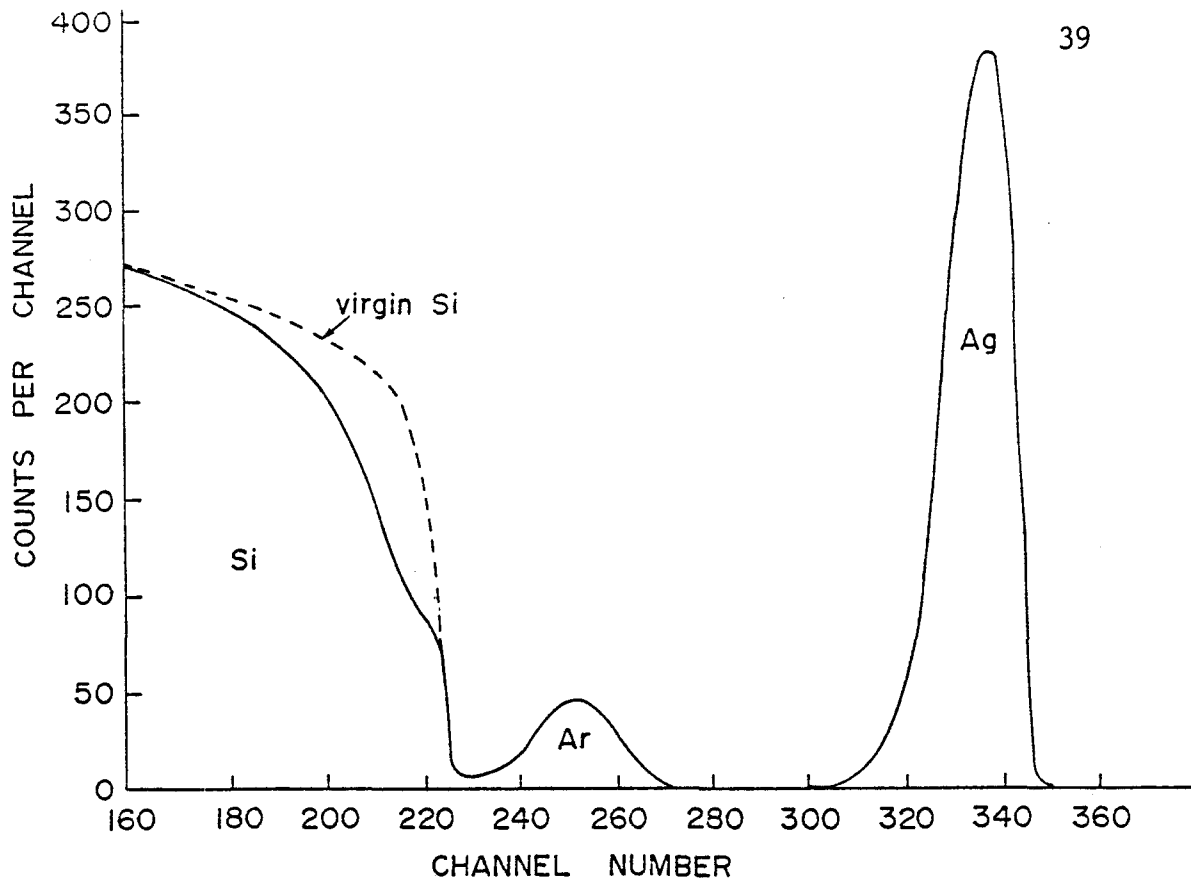


FIGURE 9: RBS Spectrum of AG on Si, after 6×10^{14} ions/mm² of 35keV Ar⁺

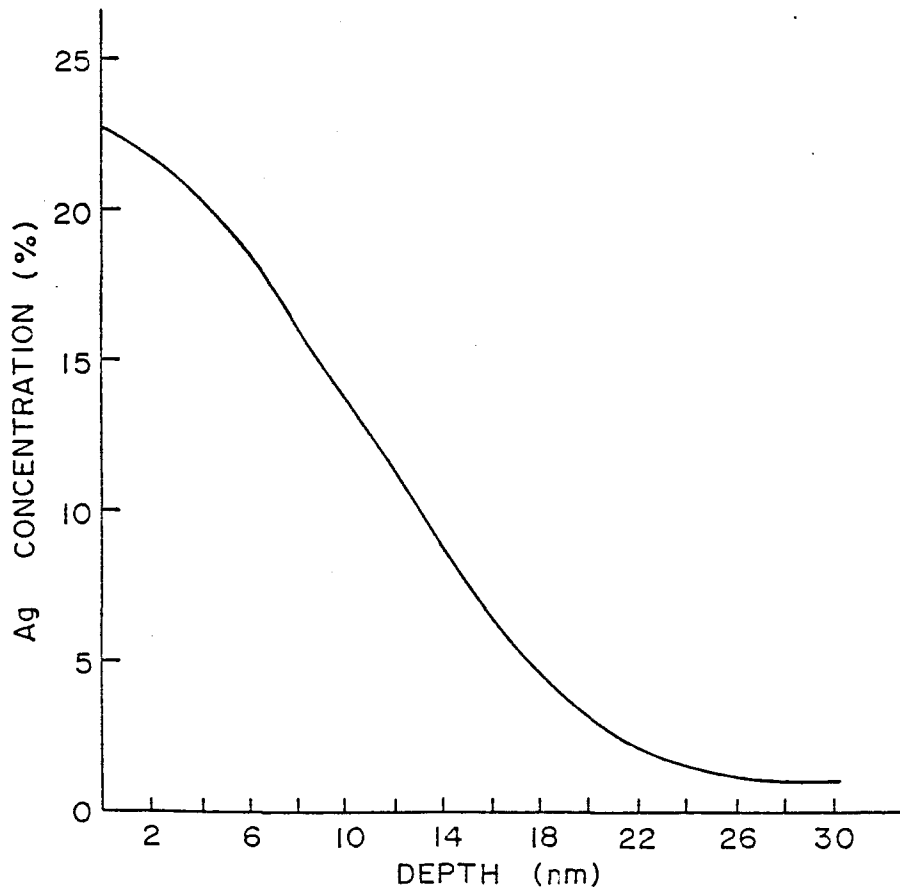


FIGURE 10: Estimated Depth Profile of Ag in Si after 6×10^{14} ions/mm² of 35keV Ar⁺

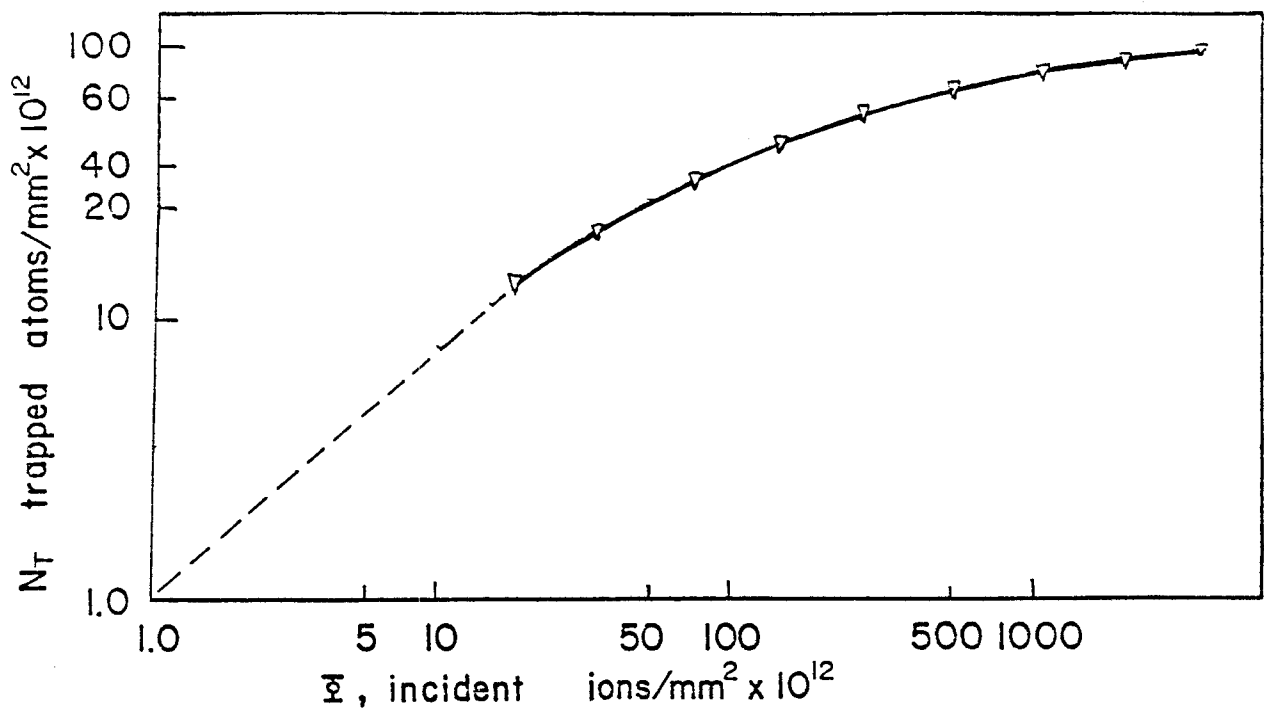


FIGURE 11: Collection Curve of 20keV Kr⁺ in Ni

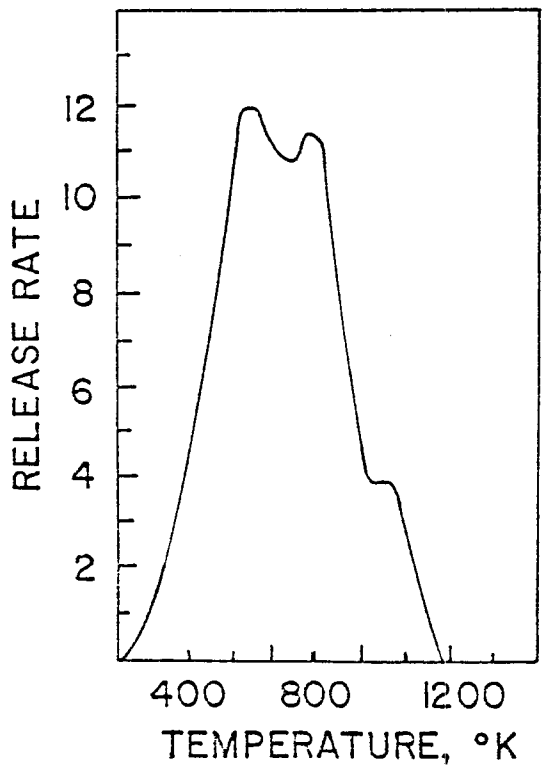


FIGURE 12: Desorption Spectrum of 500eV Ar⁺ Implanted into Ni

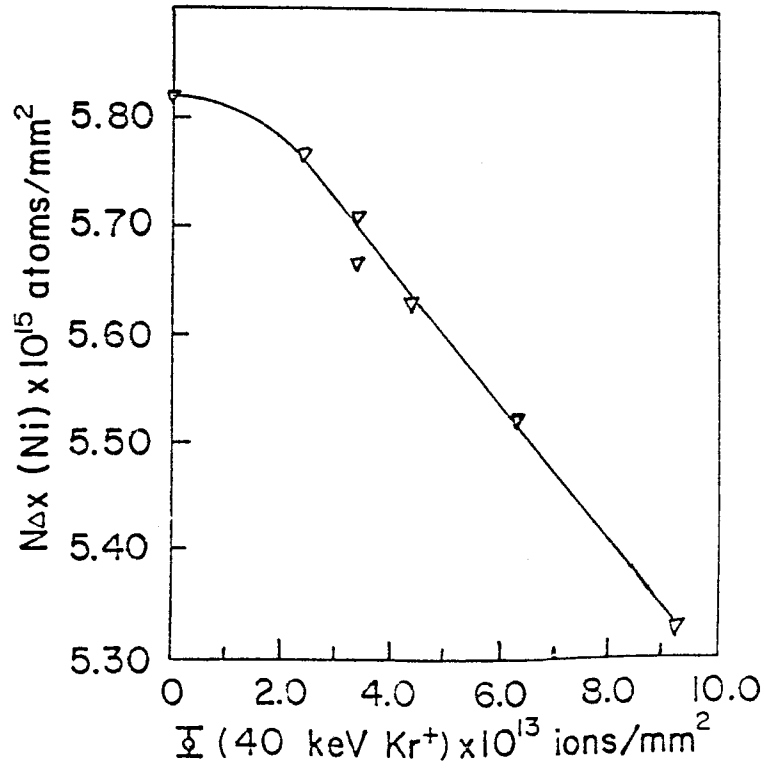


FIGURE 13: Sputtering of Ni with 40keV Kr⁺, McMaster

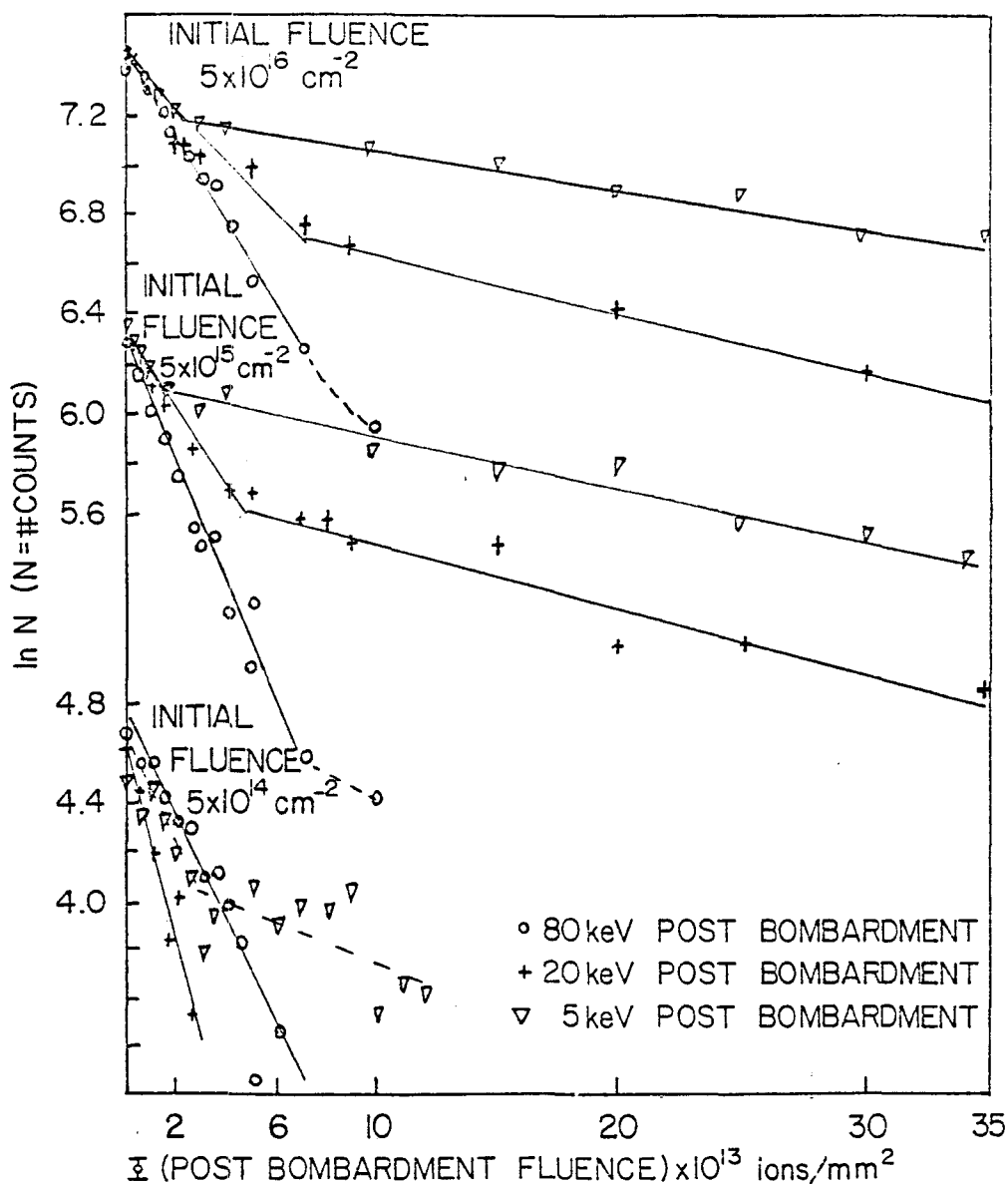


FIGURE 14: $^{85}\text{Kr}^*$ Release by Kr^+ Post-Bombardment

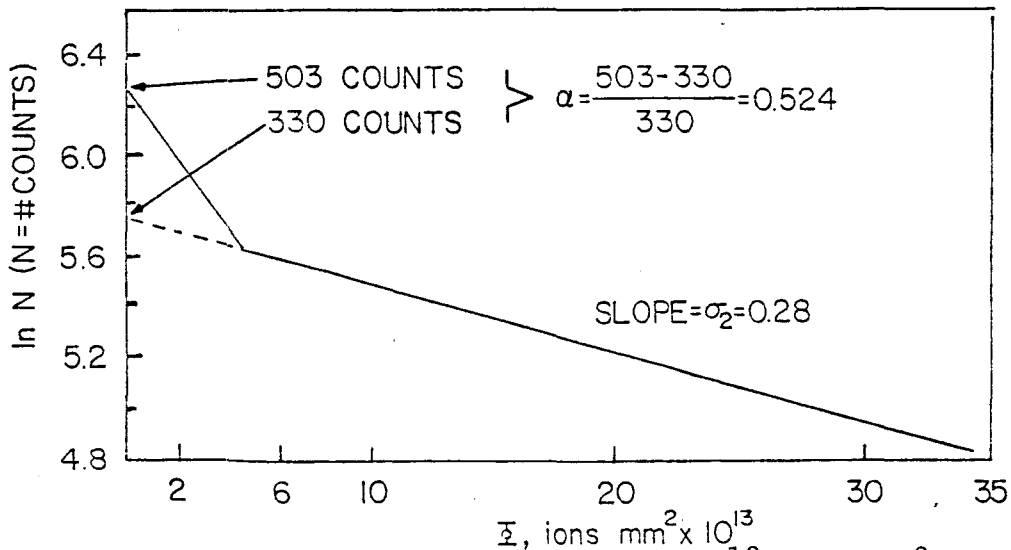


FIGURE 15: 20keV Post-Bombardment of 5×10^{13} ions/ mm^2 Implant

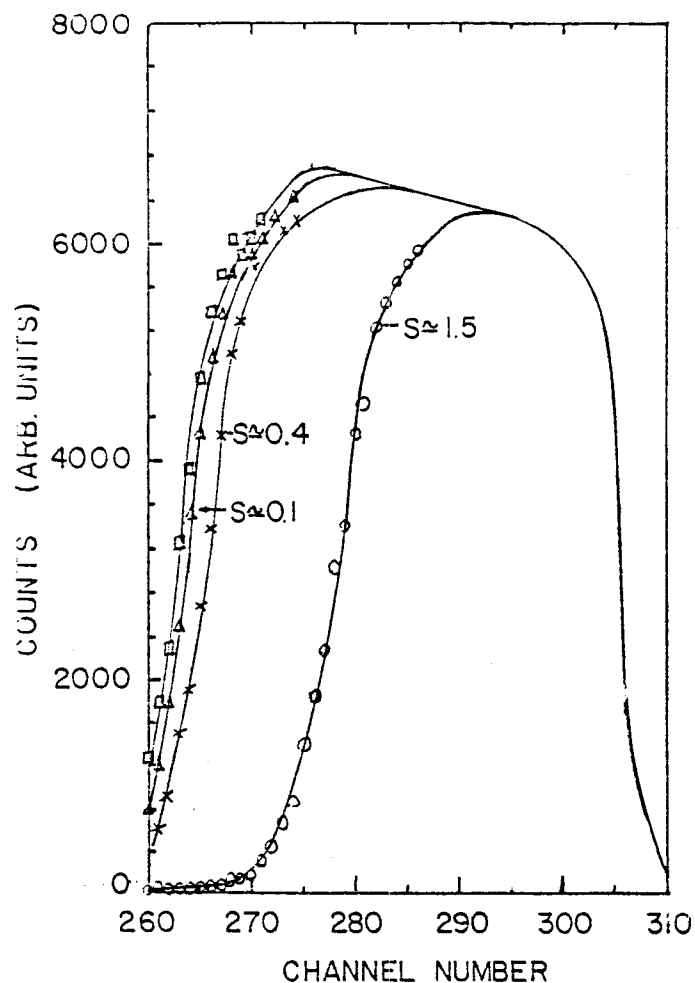


FIGURE 16: Sputtering of Ni with 40keV Kr^+ , Salford

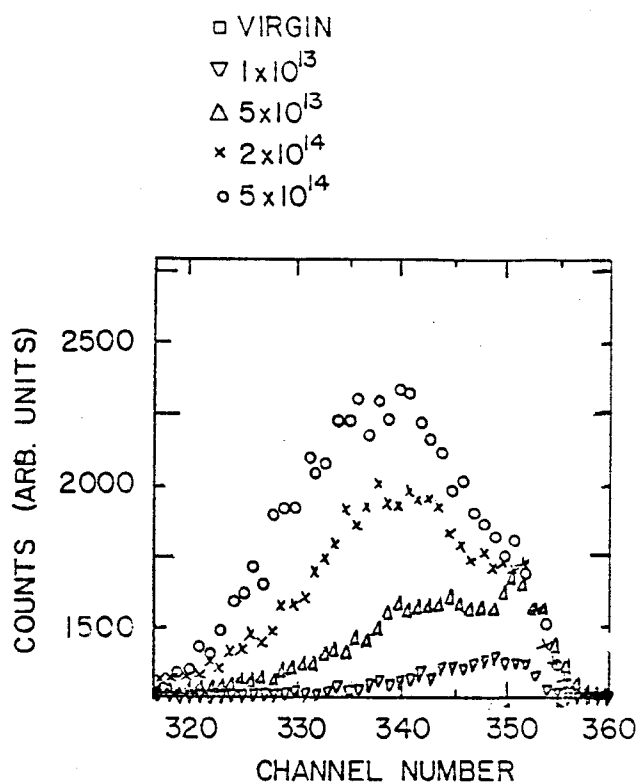


FIGURE 17: RBS Spectra of 40keV Xe^+ in Ni

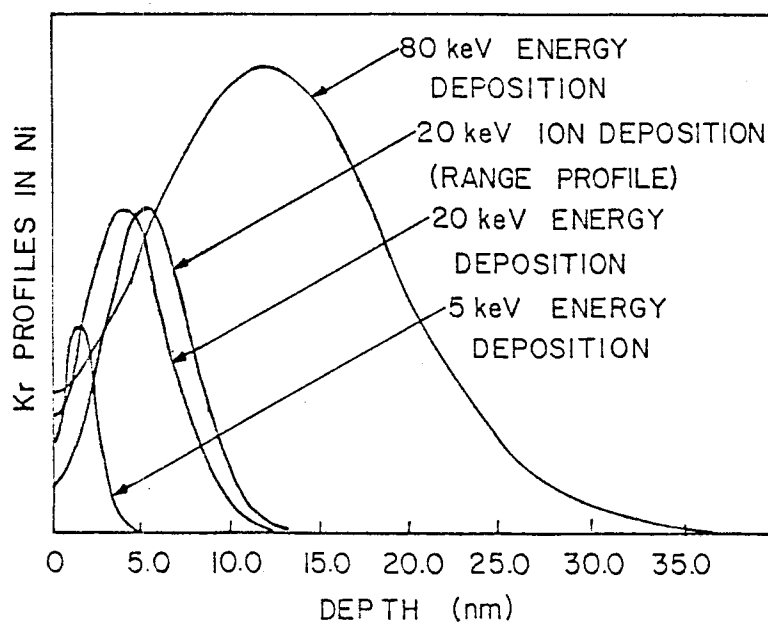


FIGURE 18: Kr^+ Ion Profiles in Ni (Winterbon Calculations)

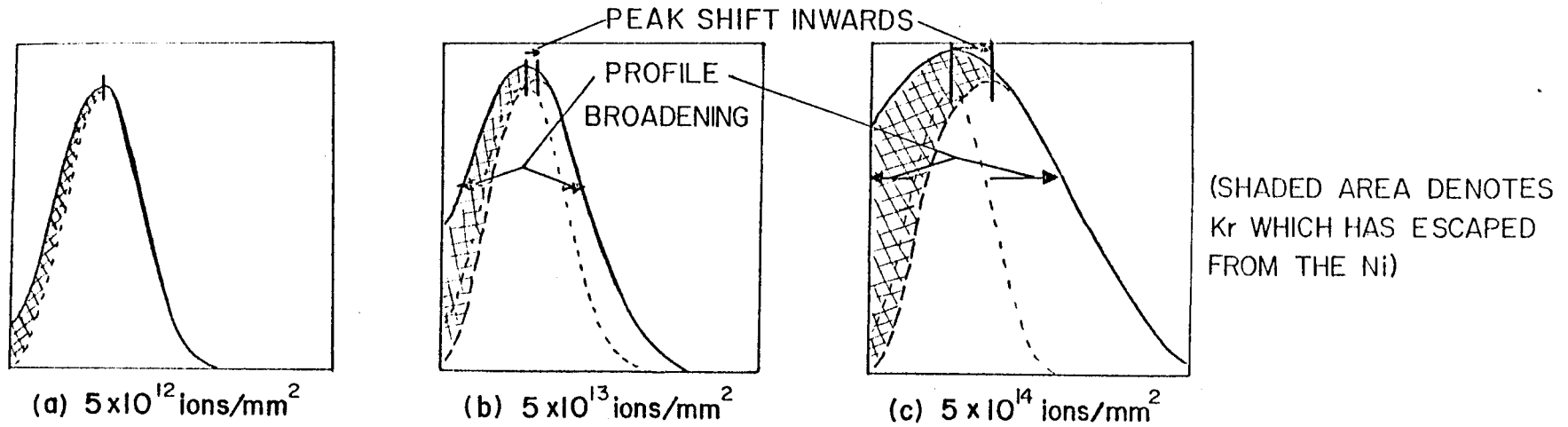


FIGURE 19: Changes in Trapped Rare Gas Profiles with Implant Fluence

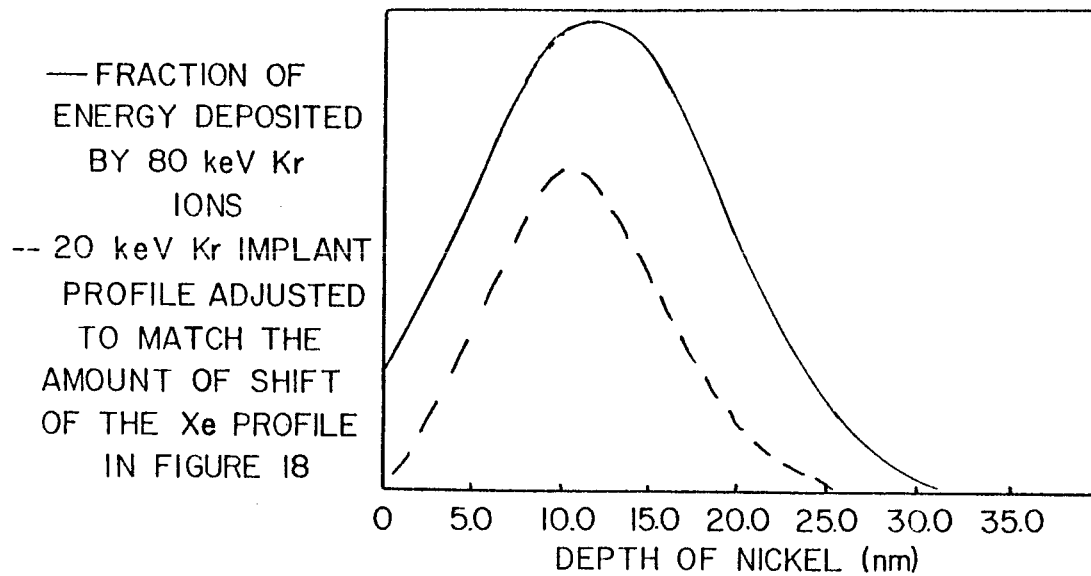


FIGURE 20: Comparison of 80keV Kr⁺ Energy Deposition Profile with Adjusted 20keV Kr⁺ Ion Deposition Profile

REFERENCES

- 1) P. Blank and K. Wittmaack, Rad. Eff. Lett. 43, 105(1979).
- 2) G. Fischer, G. Carter and R. Webb, Rad. Eff. 38, 41 (1978).
- 3) A.D. Marwick and R.C. Piller, Rad. Eff. 33, 245 (1977).
- 4) G. Carter, D.G. Armour, D.C. Ingram, R. Webb and R. Newcombe, Rad. Eff. Lett 43, 217 (1979).
- 5) U. Littmark and P. Sigmund, J. Phys. D 8, 241 (1975).
- 6) R. Grotzschel, R. Klages, U. Kreissig and A. Schmidt, Rad. Eff. 36, 129 (1978).
- 7) P. Sigmund, Rev. Roum. Phys. 17, 823 (1972).
- 8) P.K. Haff and Z.E. Switkowski, J. Appl. Phys. 18, 131 (1977).
- 9) H.H. Andersen, Appl. Phys. 18, 131 (1977).
- 10) B.Y. Tsaur, S. Matteson, G. Chapman, Z. L. Liaw, and M.A. Nicolet, Appl. Phys. Lett. 35, 825 (1979).
- 11) J. M. Walls, D. D. Hall, D. G. Teer and B. L. Delcea, Thin Solid Films 54, 303 (1978).
- 12) R. S. Nelson, 1977 Proc. Int. Conf. on Ion Plating and All. Tech.
- 13) D. G. Armour , G. Carter, R. Webb, D. C. Ingram and R. Newcombe Rad. Eff. Lett. 50, 45 (1980).
- 14) N. A. G. Ahmed, M. Sc. Thesis, U. of Salford, 1974.
- 15) R. Newcombe, C. E. Christodoulides, G. Carter and P. Tognetti, Rad. Eff. Lett. 50, 51 (1980).
- 16) P. Townsend, J.C. Kelly and N.E. W. Hartley, "Ion Impl., Sputt. and their Appl." Academic Press, 181 (1976).
- 17) H. H. Andersen and H. Bay, Rad. Eff. 13, 67 (1972).
- 18) C. E. Christodoulides, W. A. Grant and J. S. Williams, Nucl. Instr. and Meth. 149, 219 (1978).
- 19) A. Hiraki, M. A. Nicolet, J. W. Mayer, Appl. Phys. Lett. 18 178 (1971).
- 20) G. Carter, D. G. Armour, S. E. Donnelly, D. C. Ingram and R. Webb, Proc. Harwell conference, Sept. 1979.

- 21) D. E. Rimmer and A. H. Cottrell, *Phil. Mag.* 2, 1345 (1957).
- 22) A. Anderson and W. G. Gehman, *Phys. Stat. Sol.* 30, 283 (1968).
- 23) W. D. Wilson and R. A. Johnson "Interatomic Pot. and Sim. of Pt. Defects", edited by P. Gehlen, Plenum Press, N.Y., N.Y., 1972.
- 24) D. C. Ingram, private communication, 1979.
- 25) S. E. Donnelly, D. C. Ingram, R. Webb and D. G. Armour, *Vacuum* 29, 303 (1979).
- 26) G. Carter, D. G. Armour, S. E. Donnelly, D. C. Ingram and R. Webb, to be published.
- 27) R. Kelly and N. Z. Lam, *Rad. Eff.* 19, 39 (1973).
- 28) K. B. Winterbon, "Ion Impl. Range and Energy Dep. Dist." IFL/Plenum Press, 1975.
- 29) G. Carter, J. A. Baruch and W. A. Grant, *Rad. Eff.* 16, 107 (1972).
- 30) J. L. Ecuyer, M. Matsunami, J. A. Davies, *Nucl. Instr. & Math.* 160, (2); (1979) 337.
- 31) A. Hiraki, E. Lugajjo, M. A. Nicolet, and J. W. Mayer, *Phys. Stat. Sol.* (a) 7, 401 (1971).